Mapping the unique and shared functions of oncogenic KRAS and RIT1 with proteome and transcriptome profiling

April Lo[1,2]*, Kristin Holmes[1,2]*, Filip Mundt[3,4,5], Sitapriya Moorthi[1], Iris Fung[3], Shaunt Fereshetian[3], Jackie Watson[3], Steven A. Carr[3], Philipp Mertins[3,6], Alice H. Berger[1,2]

1. Human Biology Division, Fred Hutchinson Cancer Research Center, Seattle, WA, USA
2. Genome Sciences Department, University of Washington, Seattle, WA, USA
3. Proteomics Platform, Broad Institute of MIT and Harvard, Cambridge, MA, USA
4. Department of Oncology-Pathology, Karolinska Institute, Stockholm, Sweden
5. Present address: Novo Nordisk Foundation center for Protein Research, Clinical Proteomics, University of Copenhagen, Denmark
6. Present address: Proteomics Platform, Max Delbrück Center for Molecular Medicine in the Helmholtz Society, Berlin, Germany

corresponding author(s): Alice Berger (ahberger@fredhutch.org)

Abstract

21 Aberrant activation of RAS oncogenes is prevalent in lung adenocarcinoma, with somatic

22 mutation of *KRAS* occurring in ~30% of tumors. Recently, we identified somatic mutation of the

23 RAS-family GTPase *RIT1* in lung adenocarcinoma, but relatively little is known about the

24 biological pathways regulated by RIT1 and how these relate to the oncogenic KRAS network.

25 Here we present quantitative proteomic and transcriptomic profiles from *KRAS*-mutant and

26 *RIT1*-mutant isogenic lung epithelial cells and globally characterize the signaling networks

27 regulated by each oncogene. We find that both mutant KRAS and mutant RIT1 promote S6

28 kinase, AKT, and RAF/MEK signaling, and promote epithelial-to-mesenchymal transition and

29 immune evasion via HLA protein loss. However, KRAS and RIT1 diverge in regulation of

30 phosphorylation sites on EGFR, USO1, and AHNAK proteins. The majority of the proteome

31 changes are related to altered transcriptional regulation, but a small subset of proteins are

32 differentially regulated by both oncoproteins at the post-transcriptional level, including

33 intermediate filament proteins, metallothioneins, and MHC Class I proteins. These data provide

34 the first global, unbiased characterization of oncogenic RIT1 network and identify the shared

35 and divergent functions of oncogenic RIT1 and KRAS GTPases in lung cancer.

Introduction

38 Somatic mutation of the *KRAS* proto-oncogene is a prevalent feature of human cancers,

39 particularly in lung adenocarcinomas where *KRAS* is mutated in up to 30% of tumors. Cancer-

40 associated variants such as G12V and Q61H alter the normal regulation of KRAS GTPase

41 activity by disrupting GTP hydrolysis activity or physical interaction with GTPase-activating

42 proteins (GAPs)[1,2], resulting in heightened downstream cellular signaling through the canonical

43 RAS effector pathways RAF/MEK and PI3K/AKT as well as others. Following the discovery of

44   cancer-associated RAS mutations in the 1980s[3,4], thousands of studies have delineated the

45   critical pathways involved in RAS-mediated cellular transformation, metastasis, and metabolism.

46

47   Recently, another RAS-family GTPase gene, *RIT1*, was found to harbor somatic mutations in

48   lung cancer[5] and myeloid leukemias[6]. Interestingly, germline *RIT1* mutations are found in

49   families with Noonan Syndrome, a developmental "RAS"-opathy involving altered craniofacial

50   morphology and cardiac abnormalities[7], and which can also be caused by germline mutations in

51   *KRAS* itself or other RAS-pathway genes such as *SOS1, SOS2, LZTR1* and *SHOC2*

52   (https://omim.org/). In cancer and development, *RIT1* mutations are found in cases that lack

53   canonical *KRAS* mutations, suggesting that *RIT1* may impart the same phenotypes conferred by

54   activation of RAS.

55

56   Prior studies have characterized the role of RIT1 in neural development[8] and we and others

57   have described the role of mutant RIT1 in cellular transformation[5,9,10], knowledge of the function

58   of cancer- and Noonan-associated *RIT1* variants is relatively limited. Unlike *KRAS*, *RIT1*

59   mutations are rarely observed near the critical glycine residues involved in GTP hydrolysis (e.g.

60   G12 and G13 in KRAS or G30 and G31 in RIT1). Instead, *RIT1* mutations occur most frequently

61   near the switch II domain, also targeted by Q61 KRAS variants (**Fig. 1a**). Nevertheless, these

62   mutations may enhance GTP-bound levels of RIT1[11,12]. The molecular consequences of RIT1

63   switch II domain mutations may additionally be linked to the loss of RIT1's physical interaction

64   with LZTR1, a ubiquitin-conjugating enzyme responsible for degradation of RIT1[11]. Cancer- and

65   Noonan-associated RIT1 variants lose the ability to interact with LZTR1 and consequently are

66   highly overexpressed, resulting in increased signaling activity through the RAF/MEK pathway[11].

67

68   Prior studies of RIT1 function focus on candidate cellular signaling pathways based on RIT1's

69   homology to KRAS. To our knowledge, unbiased mapping of downstream RIT1-regulated

70   pathways has not been performed to date. Here we sought to broadly describe the proteome,

71   phosphoproteome, and transcriptome changes induced by wild-type RIT1 and RIT1[M90I], a

72   cancer- and Noonan-associated variant, and to compare these changes to those induced by

73   oncogenic KRAS variants. With a particular interest in the consequences of RIT1[M90I] in lung

74   cancer, we profiled the effects of RIT1[M90I] mutation in AALE cells, a non-transformed,

75   immortalized, human lung epithelial cell line[13].

76

77   By comparing the downstream pathways regulated by oncogenic KRAS and RIT1, we uncover

78   previously unknown consequences of RIT1 activation, such as induction of the epithelial-to-

79   mesenchymal transition (EMT) and post-translational regulation of HLA protein expression. In

80   addition, we uncover additional functional differences between KRAS and RIT1 including a

81   distinct and unique role of KRAS mutants in regulation of EGFR and USO1 phosphorylation.

82   These data provide the first systems-level view of RIT1 and RIT1[M90I] function.

83

84   Results

85

86   **Multi-omic profiling of RIT1- and RAS-transformed human lung epithelial cells**

87   We previously demonstrated that RIT1[M90I] and other cancer-associated RIT1 variants can

88   promote cellular transformation of NIH3T3 cells in vitro and in vivo[5]. To determine whether

89   RIT1[M90I] was capable of transforming human lung epithelial cells, we expressed mutant RIT1 or

90   KRAS in the human lung epithelial cell line, AALE. Similar to our previous findings in rodent

91   cells, both RIT1[M90I] and KRAS[G12V] enabled AALE cells to form colonies in soft agar (**Fig. 1b**).

92

4

93 The canonical function of oncogenic RAS variants is the downstream activation of the

94 RAF/MEK/ERK cellular signaling cascade[14], and RIT1 shares the ability to bind C-RAF and

95 induce transcription of ERK target genes activity[11]. To determine if such regulation is active in

96 AALE cells, we stably expressed wild-type RIT1 or KRAS, or the mutant forms RIT1[M90I],

97 KRAS[G12V], and KRAS[Q61H] in AALE cells. KRAS[Q61H] was included since this mutant more closely

98 resembles the switch II domain mutants observed in *RIT1* in cancer (**Fig. 1a**). RIT1[M90I],

99 KRAS[G12V], and KRAS[Q61H] all enhanced ERK phosphorylation compared to their respective wild-

100 type protein or vector control (**Fig. 1c**). Interestingly, wild-type RIT1 overexpression also

101 modestly enhanced ERK phosphorylation whereas wild-type KRAS suppressed basal ERK

102 phosphorylation.

103

104 To systematically characterize the signaling networks perturbed by mutant RIT1 and KRAS in

105 lung cancer, we expressed each variant in AALE cells and performed both RNA-seq and deep

106 proteome and phosphoproteome profiling by liquid chromatography tandem mass spectrometry

107 (LC-MS/MS). Following trypsin digestion, peptides were labeled with tandem mass tag (TMT)

108 reagents in two overlapping 10-plex sets for relative quantification of proteome and

109 phosphopeptides by LC-MS/MS (**Fig. 1d and Supplementary Fig. 1a-b**). Following basic

110 reverse phase chromatography, fractions were either directly subjected to LC-MS/MS for total

111 proteome quantification, or subjected to immobilized metal affinity chromatography (IMAC) to

112 enrich for phosphopeptides and then subjected to LC-MS/MS, or. In total, we identified 10,131

113 proteins, 9002 of which were detected and quantified in every sample, and 29,140

114 phosphopeptides, 12,325 of which were identified in common in every sample (**Supplementary

115 Tables 1 and 2 and Supplementary Files 1 and 2**).

116

117   In parallel, we generated deep transcriptome profiles of the same isogenic cell lines.

118   Transcriptome profiling was performed in triplicate on the Illumina NovaSeq platform to a

119   median read-depth per replicate of 70.1 million reads (**Fig. 1e**, **Supplementary Table 3 and**

120   **Supplementary Fig. 1e**). No compensatory feedback regulation of RIT1 to KRAS or vice versa

121   was observed (**Fig. 1f**). Despite relatively low protein expression of KRAS variants in the AALE

122   lines (**Fig. 1c**), the majority of KRAS transcripts in each isogenic cell line corresponded to G12V

123   or Q61H variants, respectively, with 84.1% of reads harboring the G12V variant in KRAS^{G12V}

124   cells, and 73.3% of reads corresponding to the Q61H allele in KRAS^{Q61H} cells (**Fig. 1g**). As

125   expected, known KRAS-regulated gene sets were strongly up- and down-regulated in KRAS-

126   mutant cells (**Supplementary Fig. 1d**).

127

128   **Multi-omic profiling identifies global similarity between signaling regulated by RIT1^{M90I}**

129   **and oncogenic KRAS**

130   Differentially abundant proteins were identified by comparison to the vector control cells using a

131   two-tailed moderated t-test (**Fig. 2a**). Selected proteins observed to be significantly modulated

132   by LC-MS/MS were cross-validated by Western blot. FOSL1, also known as FRA1, is a basic

133   leucine zipper transcription factor in the FOS family[15]. Activation of RAS is known to promote

134   transcriptional upregulation and protein stabilization of FOSL1[16,17]. By LC-MS/MS, FOSL1 was

135   markedly overexpressed in KRAS^{G12V}, KRAS^{Q61H}, and RIT1^{M90I}-mutant cells compared to wild-

136   type cells or vector control cells (**Fig. 2b**). Consistently, Western blot of independently-derived

137   AALE isogenic lines demonstrated greater abundance of FOSL1 in KRAS- or RIT1-mutant cells

138   compared to wild-type expressing cells (**Fig. 2b**). TXNIP is an inhibitor of thioredoxin involved in

139   both redox regulation and glucose metabolism[18,19]. Prior literature identified HRAS^{G12V}-induced

140   suppression of TXNIP transcription and protein translation[20,21]. TXNIP was among the top down-

141   regulated proteins in KRAS- and RIT1-mutant proteomes, and was decreased in Western blot

142   analysis of independently derived cells (**Fig. 2c**). These validation data demonstrate the utility of

143   LC-MS/MS to describe protein expression changes and additionally suggest the mechanism of

144   RAS-mediated modulation of FOSL1 and TXNIP is shared with RIT1^{M90I}.

145

146   Next we compared the global effects of RIT1^{WT} and RIT1^{M90I} to that of KRAS^{WT} and KRAS

147   variants. Proteome and phosphoproteome data from RIT1^{M90I}-expressing cells were highly

148   correlated with KRAS^{G12V} and KRAS^{Q61H} profiles, suggesting largely similar downstream

149   consequences (r = 0.70-0.80 and 0.72-0.75 for proteome and phosphoproteome, respectively;

150   **Fig. 2d**). Despite differences in KRAS protein abundance, KRAS^{G12V} and KRAS^{Q61H} proteomes

151   and phosphoproteomes were highly correlated (proteome r = 0.85 and phospho r = 0.79; **Fig.**

152   **2d**). In contrast, wild-type KRAS replicates were the most divergent of all profiles, showing

153   limited correlation to either the KRAS-mutant profiles or RIT1 profiles.

154

155   A recent study found that RIT1 variants, including M90I, may function by relieving negative

156   regulation of RIT1 by a LZTR1-dependent proteasomal degradation mechanism[11]. Accordingly,

157   overexpression of wild-type RIT1 should largely phenocopy expression of RIT1^{M90I}. Consistent

158   with this idea, RIT1^{WT} cells more closely resembled both RIT1^{M90I} and KRAS-mutant cells than

159   KRAS^{WT} cells (**Fig. 2d**). These data highlight a critical divergence between KRAS and RIT1:

160   expression of wild-type KRAS is not capable of activating downstream oncogenic pathways,

161   whereas expression of wild-type RIT1 in part resembles activation of RIT1 or KRAS by

162   mutation. We confirmed this observation in a principal component analysis of transcriptome

163   data, which further revealed a high degree of similarity between RIT1^{WT} and RIT1^{M90I}-regulated

164   gene expression (**Fig. 2e and Supplementary Table 4**).

165

166

167   **Oncogenic RIT1 promotes epithelial-to-mesenchymal transition**

168   To identify the downstream pathways regulated by oncogenic KRAS and RIT1, we performed

169   gene set overlap analysis using MSigDB Hallmark Pathway gene sets[22] (**Fig. 3a**). The epithelial-

170   to-mesenchymal transition (EMT) pathway was the most significant gene set enriched among

171   up-regulated proteins for both KRAS[G12V]/KRAS[Q61H] and RIT1[WT]/RIT1[M90I] cell lines. EMT is a

172   cellular transdifferentiation process promoted by cell-extrinsic signaling proteins and

173   orchestrated by activation of transcription factors such as Twist, Snail, and Zeb family

174   transcription factors[23]. It has long been observed that oncogenic RAS proteins, including KRAS

175   mutants, promote EMT. An EMT-signature is associated with KRAS dependence[24], which has

176   been functionally linked to activation of FOSL1[25]. Interestingly, we find both RIT1[M90I] and

177   KRAS[G12V]/KRAS[Q61H] are capable of promoting expression changes of key EMT markers,

178   including up-regulation of Vimentin, N-Cadherin, and Fibronectin, and downregulation of Keratin

179   19 (**Fig. 3b and Supplementary Fig. 2a**). Although canonical EMT transcription factors Snail

180   (SNA1) and Slug (SNA2) were not detected by proteomic analysis, transcriptomes from RIT1-

181   and KRAS-mutant cells showed increased activity of these EMT transcription factors as

182   determined by ChEA3 transcription factor enrichment analysis (**Fig. 3c-d and Supplementary**

183   **Fig. 2b**). To our knowledge, this is the first demonstration of mutant RIT1 promoting EMT in any

184   cell type.

185

186   **Oncogenic KRAS and RIT1 suppress Class I MHC expression via a post-transcriptional**

187   **mechanism**

188   Among the top suppressed proteins with differential abundance in both mutant KRAS and

189   RIT1[M90I] cells, were major histocompatibility complex (MHC) proteins. Class I MHC proteins

190   HLA-A, HLA-B, HLA-C, and HLA-F were potently suppressed by KRAS[G12V], KRAS[Q61H], and

191   RIT1[M90I] (**Fig. 4a-b and Supplementary Fig. 3a**). Recently there has been a renewed interest

8

192   in expression of immune modulatory proteins in cancer due to the appreciation of the potent role

193   of the immune system in shaping cancer evolution. Further understanding the regulation of HLA

194   expression in cancer is particularly critical in metastatic *KRAS*-mutant lung adenocarcinoma,

195   where chemotherapy combined with immune checkpoint blockade is often used in the first-line

196   setting.

197

198   Class I MHC genes *HLA-A, HLA-B*, and *HLA-C* harbor loss-of-function mutations in cancer[26],

199   demonstrating selective pressure to lose MHC function during tumorigenesis. Both MHC

200   expression loss and upregulation of the immune suppressive protein PD-L1 enable tumor

201   evasion of T-cell recognition of aberrant cancer cell proteins[27]. Moreover, expression loss of

202   HLA proteins or B2M, another MHC Class I complex protein, is associated with resistance to

203   immunotherapy in cancer[28]. We found that RIT1^{M90I}, KRAS^{G12V}, and KRAS^{Q61H} cells all promoted

204   loss of B2M protein abundance in addition to HLA protein loss (**Fig. 4c**).

205

206   Class I MHC expression is known to be dynamically regulated by upstream signals controlled by

207   interferon gamma exposure, NF-kB signaling, and chromatin regulators such as EZH2[29,30]. Each

208   of these mechanisms involves transcriptional regulation of class I MHC genes. However, there

209   were no transcriptional differences in HLA genes in the KRAS-mutant and RIT1-mutant cells nor

210   were any transcriptional differences observed in the upstream regulators of MHC Class I

211   expression NLRC5 and IRF1 and IRF2 (**Supplementary Fig. 3b**). Moreover, we excluded the

212   possibility that lentiviral transduction or expression of a foreign antigen was responsible for the

213   HLA suppression, because HLA protein expression was maintained or enhanced in RIT1^{WT}-

214   expressing cells as well as vector control cells, which express the Renilla luciferase gene.

215

216   To identify the possible mechanism of RIT1[M90I]- and KRAS-mediated MHC suppression, we

217   identified other proteins that, like HLA, were upregulated in RIT1[WT] cells but suppressed in

218   RIT1-mutant and KRAS-mutant cells (**Fig. 4d**). This analysis revealed the pervasive

219   downregulation of the Rab-mediated ER/Golgi vesicle-trafficking pathway that controls MHC

220   Class I processing and presentation as well as the MHC Class I complex proteins themselves

221   (**Fig. 4e**). In addition, expression of the proteasomal subunit PSMB9 correlated with loss of the

222   MHC processing machinery (**Fig. 4f and Supplementary Fig. 3c**). Loss of PSMB9, also known

223   as LMP2, has been previously linked to loss of MHC expression after oncogenic

224   transformation[31]. We conclude that RIT1[M90I] and KRAS[G12V]/KRAS[Q61H] suppress MHC Class I

225   expression through a post-transcriptional mechanism possibly involving PSMB9. Further

226   investigation of MHC Class I expression loss driven by these oncogenic RIT1 and KRAS is

227   critical to better understand the role of RAS and RIT1 signaling on immune evasion in cancer.

228

229   The identification of a major class of proteins regulated at the post-transcriptional level in RIT1-

230   and KRAS-transformed lung epithelial cells brought to our attention the possibility of other post-

231   transcriptional regulation by RIT1 and KRAS. Indeed, oncogenic RAS signaling profoundly

232   alters cap-dependent translation via activation of the p90 ribosomal S6 kinases (RSKs)[32] and

233   PI3K/mTOR[33], so differential protein translation could significantly contribute to altered protein

234   abundance in RAS-transformed cells. To determine whether there were other protein classes in

235   addition to MHC Class I proteins with significant post-transcriptional regulation, we performed a

236   global correlation analysis of the transcriptome and proteome. Significant linear correlations

237   between transcript and protein abundance were observed for RIT1 and KRAS variants, with the

238   correlation highest for cells expressing mutant KRAS[G12V] ($r = 0.3725$) or KRAS[Q61H] ($r = 0.3620$)

239   (**Fig. 4g**). While expression of the majority of genes were correlated at the RNA and protein

240   levels, the metallothionein protein family including MT1E, MT1F and MT1X was highly

241   upregulated in the proteome but not transcriptome of KRAS-mutant cells (**Fig. 4g**). In addition,

242   intermediate filament proteins were also substantially regulated post-transcriptionally; both

243   alpha-internexin (INA) and vimentin (VIM) were expressed more highly in the proteome than

244   expected from RNA-seq data (**Fig. 4g**). These data highlight the utility of LC-MS/MS to identify

245   protein abundance changes that would not be predicted from transcriptome analysis.

246

247   **Phosphoproteome profiling illuminates shared and unique signaling by RIT1 and KRAS**

248   Protein phosphorylation is a reversible and dynamic mechanism of intracellular signaling that

249   enables rapid intracellular transduction of signals controlling cell proliferation, survival, and

250   metabolism. Although both RIT1 and KRAS act as GTPase switches, they both stimulate

251   activation of cellular protein kinases such as BRAF. We therefore evaluated protein

252   phosphorylation regulated by wild-type and mutant RIT1 and KRAS. Phosphosite abundance

253   was expressed as a relative abundance normalized to the total protein abundance for each

254   phosphoprotein. Unsupervised hierarchical clustering of the phospho-signatures identified the

255   RIT1^{M90I} phosphoproteome as most similar to KRAS^{G12V} and KRAS^{Q61H} phospho-signatures

256   (**Supplementary Fig. 4a**). We performed Kinase-Substrate Enrichment Analysis (KSEA[34]),

257   which uses kinase-substrate pairings from PhosphoSitePlus[35] and NetworKIN[36] to identify

258   differential phosphorylation of kinase-substrate families (**Supplementary Table 5**). These data

259   further confirmed the similarity in phosphorylation state between RIT1-mutant and KRAS-mutant

260   cells. The top kinases with increased substrate phosphorylation in RIT1-mutant and KRAS-

261   mutant cells were ribosomal S6 kinase (RPS6KA1), Protein kinase C (PRKCA), AKT1, and

262   MAPKAPK2 (**Fig. 5a-c**, **Supplementary Fig. 4b-e,** and **Supplementary Table 5**). The levels of

263   phosphorylation of RPS6KA1 and MAPKAPK2 substrates were enhanced most strongly in the

264   mutant cells and less in RIT1 WT and KRAS WT-expressing cells (**Fig. 5b-c**). Substrates of

265   Aurora kinase B and CDK1 and PAK1 were suppressed in RIT1- and KRAS-mutant cells (**Fig.**

266   **5a** and **Supplementary Fig. 4b-c and Supplementary Fig. 4f)**. Although the total

267   phosphorylation of each substrate reflects the balance between kinases and phosphatases in

268   the cell, these data suggest that RIT1^{M90I}, like oncogenic KRAS, can activate the canonical RAS

269   effector pathways involving S6 kinase and AKT.

270

271   Next we assessed the divergent functions of RIT1^{M90I} and KRAS^{G12V}/KRAS^{Q61H} by identifying

272   proteins with differential phosphorylation in KRAS-mutant versus RIT1^{M90I}-mutant cells. 902

273   differentially phosphorylated sites were identified by two-tailed t-test and multiple hypothesis

274   correction (**Fig. 5d; FDR < 0.05).** Interestingly, the top site with lower phosphorylation in

275   KRAS^{G12V} and KRAS^{Q61H} cells was EGFR serine 1026 (**Fig. 5d**). In lung adenocarcinoma, *KRAS*

276   mutations and *EGFR* mutations are mutually exclusive, suggesting a powerful genetic

277   interaction between these two genes. Recent work demonstrated that mutant KRAS and EGFR

278   display synthetic lethality[37]. However the mechanism underlying this lethality is unknown.

279   Further inspection of the phospho-proteome signatures revealed extensive alteration of EGFR

280   phosphorylation by KRAS^{G12V} and KRAS^{Q61H}, but not by RIT1^{M90I}. 11 of 12 EGFR sites detected

281   by LC-MS/MS occur in the cytoplasmic carboxy-terminal tail of EGFR (**Fig. 5e**). Five of these

282   sites (S991, S991/T993 double phosphorylation, S1026, S1039, and T1041/S1045 double

283   phosphorylation) were significantly depleted of phosphorylation in KRAS^{G12V} and KRAS^{Q61H}-

284   expressing cells but not in RIT1^{M90I}-expressing cells. Interestingly, these sites lie in a region of

285   EGFR that is involved in receptor internalization and endocytosis[38] and a phosphorylation-

286   deficient mutant at S991 is defective at internalization[39]. Consistently, EGFR protein abundance

287   was increased in KRAS-mutant cells (**Supplementary Fig. 4g**) Although the specific regulatory

288   mechanisms leading to this depletion remain unknown, these data point to the existence of

289   feedback regulatory signaling from oncogenic KRAS to EGFR.

290

291   Examining phosphorylation uniquely promoted by KRAS[G12V] and KRAS[Q61H], we identified USO1

292   phosphorylation at S48 as one of the top most significantly increased phosphorylation events in

293   KRAS-mutant cells. USO1, also known as p115, is a vesicle tethering factor involved in ER-

294   Golgi intracellular trafficking[40]. Although wild-type KRAS and KRAS-mutant proteomic

295   signatures were largely divergent, USO1 serine 48 phosphorylation was promoted by both

296   KRAS[WT] and mutant KRAS (**Fig. 5f**). KRAS relies on vesicle trafficking to ensure proper post-

297   translational farnesylation and palmitoylation, which are required for targeting of KRAS to the

298   plasma membrane[41]. We hypothesized that USO1 S48 phosphorylation was therefore

299   correlated with KRAS expression rather than activity. Indeed, a significant correlation was

300   observed between overall KRAS expression and USO1 phosphorylation (**Fig. 5g**). In contrast,

301   USO1 S48 phosphorylation was only modestly changed in RIT1-mutant cells (**Fig. 5d**). Notably,

302   RIT1 lacks the farnesylation and palmitoylation signals present in RAS isoforms[42], so the

303   differential regulation of USO1 by KRAS and RIT1 may be related to differences in RIT1 and

304   KRAS trafficking.

305

306   Also among the top differentially phosphorylated sites were 32 phosphorylation sites in AHNAK

307   proteins 1 and 2. AHNAK and AHNAK2 are large scaffolding proteins that have been implicated

308   as tumor suppressor proteins in breast and lung cancer[43,44]. Among all phospho-proteins, a

309   higher proportion (32/117) of sites on AHNAK and AHNAK2 were differentially phosphorylated

310   than expected by chance (P < 0.0001 by Chi Square test; **Supplementary Fig. 4h**). Intriguingly,

311   two recent proximity-labeling proteomic studies identified AHNAK and AHNAK2 as KRAS-

312   interacting proteins[45,46], raising the possibility that a direct physical interaction between KRAS

313   and AHNAK proteins may be involved in the differential AHNAK phosphorylation we observe.

314

Discussion

Here we describe quantitative proteomic, phosphoproteomic, and transcriptomic datasets that provide the first systematic view of the RIT1[M90I]-regulated signaling network. These datasets were generated from isogenic human lung epithelial cells to provide a physiological view of the consequences of RIT1 activation in the same cellular compartment that is involved in lung adenocarcinoma, a tumor type with prevalent mutations in *KRAS* and *RIT1*. Broadly, we find that 'omic signatures from RIT1[M90I]-expressing cells largely phenocopy those from cells with overexpression of wild-type RIT1. This finding lends further support to the notion that oncogenic RIT1 variants function at least in part through increasing RIT1 abundance[11]. This is in contrast to KRAS, where overexpression of wild-type KRAS induces signatures unrelated or opposite to that of oncogenic KRAS variants G12V and Q61H. The opposing functions of wild-type and mutant KRAS is consistent with recent evidence suggesting that KRAS functions as a dimer and that wild-type KRAS directly inhibits the function of oncogenic KRAS variants via physical dimerization[47]. This divergence in the function of wild-type RIT1 and KRAS hints at fundamental differences in molecular regulation of each wild-type GTPase. The ability of RIT1 to promote downstream RAF/MEK/ERK signaling when aberrantly expressed suggests that RIT1 may not be subject to the same tight regulation by GTPase-activating proteins (GAPs) that normally keep RAS in an inactive state. Furthermore, these data raise the possibility that wild-type RIT1 overexpression in *RIT1*-amplified cancers may contribute to tumorigenesis. *RIT1*, on chromosome 1q, is frequently amplified in uterine carcinosarcoma, liver hepatocellular cancer, cholangiocarcinoma, breast cancer, lung adenocarcinoma, and ovarian cancer. RIT1 mRNA expression is increased in amplified cases, regardless of tissue type, raising the possibility that RIT1 overexpression could play a role in tumorigenesis in these cancers.

14

340   We find that RIT1^{M90I}, KRAS^{G12V}, and KRAS^{Q61H} share the ability to activate canonical RAS

341   effector pathways PI3K/AKT and RAF/MEK. Likely as a consequence of RAF/MEK signaling to

342   FOSL1, RIT1^{M90I} also shares the ability to induce EMT markers including Vimentin, N-cadherin,

343   and fibronectin. KRAS and RIT1 variants also shared the ability to profoundly suppress HLA-A, -

344   B, and -C expression via a posttranscriptional mechanism. Taking advantage of differential

345   expression of HLA proteins between RIT1^{WT} and all other isogenic lines, we identified an entire

346   Rab-mediated endocytic network that was lost together with HLA proteins in RIT1- and KRAS-

347   mutant cells. This downregulated module also included PSMB9, a subunit of the

348   immunoproteasome that is involved in antigen processing for class I MHC presentation. RAS

349   oncogenes have long been recognized to suppress surface MHC expression[48], in some cases

350   transcriptionally and in others post-transcriptionally[31]. Our data link both oncogenic RIT1 and

351   RAS to modulation of the processing and trafficking of MHC Class I molecules. Further

352   identification of the mechanism of RIT1/RAS-mediated MHC suppression will provide a better

353   understanding of tumor immune evasion which is critically needed to optimize patient

354   stratification of cancer immunotherapy.

355

356   In addition to the largely concordant regulation of proteins by mutant RIT1 and KRAS, we

357   identified several unique phosphoproteins with differential abundance in RIT1^{M90I} and KRAS-

358   mutant cells. These included EGFR, a key oncoprotein in lung adenocarcinoma, which showed

359   reduced phosphorylation of sites involved in receptor internalization and endocytic trafficking.

360   Given the potent genetic interactions between KRAS and EGFR in lung cancer and colon

361   cancer, it is attractive to speculate that feedback regulation of KRAS to EGFR could provide an

362   explanatory mechanism for this phenomenon. Future work is needed to determine the basis of

363   the specific regulation of EGFR phosphorylation by oncogenic KRAS but not RIT1.

15

364   Together, these results demonstrate the power of quantitative proteomics and transcriptomics to

365   provide global views of cancer oncogene signaling. Our multi-omic analysis validated known

366   consequences of RAS activation such as EMT and activation of RAF/MEK and PI3K signaling.

367   For the first time, we gained a global view of RIT1 function, which confirmed its ability to

368   stimulate canonical RAS signaling. However, phosphoproteomic profiling identified a number of

369   key divergent mechanisms between KRAS- and RIT1-mutant cells, which point to the existence

370   of novel, unique regulators or effectors of KRAS and RIT1 still to be identified. Future work is

371   needed to investigate the mechanisms of these differences between KRAS and RIT1, the

372   results of which will have important implications for cancer therapy and Noonan Syndrome.

373
374

375
376
377

378 **Methods**

379

380 **Isogenic Cell Line Generation**

381 Plasmid constructs were cloned using Gateway Technology (Invitrogen/ThermoFisher) using

382 pLX301 destination vector (Broad Institute) and pDONR223-RIT1 donor vectors previously

383 described[5]. Lentivirus was generated by transfection of HEK293T cells with packaging and

384 envelope vectors using standard protocols. AALE cells were a kind gift of Jesse Boehm (Broad

385 Institute). Isogenic cells were generated by transduction of lentivirus generated from pLX317-

386 Renilla luciferase or pLX301-RIT1^{WT}, pLX301-RIT1^{M90I}, pLX301-KRAS^{WT}, pLX301-KRAS^{G12V}, or

387 pLX301-KRAS^{Q61H} and selection with puromycin. Stable pools of cells were maintained in small

388 airway growth medium (Lonza).

389

390 **Soft Agar Assay**

391 1×10^5 cells were suspended in 1 ml of 0.33% select agar in small airway growth medium without

392 EGF (Lonza) and plated on a bottom layer of 0.5% select agar in the same media in six-well

393 dishes. Each cell line was analyzed in triplicate. Colonies were photographed after 14–21 days

394 and quantified using CellProfiler[49].

395

396 **Transcriptome profiling**

397 Three technical replicates per cell line were harvested at ~90% confluence (n = 18 total dishes).

398 Cells were lysed and total RNA was extracted using Direct-zol RNA Miniprep plus (Zymo

399 Research). Libraries were constructed using the non-strand-specific poly-A selection Illumina

400 TruSeq kit for 50bp paired-end reads. Libraries were then pooled and sequenced on the

401 Illumina NovaSeq platform (Fred Hutch Genomics Core). Reads were aligned to the human

402 reference genome build hg19/GRCh37 using STAR v.2.5.3a[50]. Alignments were annotated for

403 duplicates and read groups, and then reordered and indexed, using Picard Tools v.1.114[51].

404 Read statistics for each RNA-seq sample were calculated using RSeQC[52]. Quantification of

405 gene transcripts was performed by the featureCounts program within the Subread package[53],

406 using hg19 gene annotation from UCSC Gene level CPM and RPKM values were calculated

407 with edgeR v.3.22.3[54], and converted into transcripts per million (TPM values with an in-house

408 script. In total, 12,887 genes were identified with average logCPM at least 0.1 across all

409 samples. Differential expression analyses comparing KRAS or RIT1 perturbed cell lines against

410 vector control lines were performed using edgeR[54].

411

412 **High performance liquid chromatography tandem mass spectrometry (LC-MS/MS)**

413 Cells were washed in ice-cold PBS, scraped into PBS, pelleted, and snap frozen in liquid

414 nitrogen. The experimental workflow for sample processing, TMT-labeling, peptide enrichment,

415 and LC-MS/MS were largely as previously described[55]. Briefly, pellets were lysed in 200 μl of

416 chilled urea lysis buffer (8 M urea, 75 mM NaCl, 50 mM Tris (pH 8.0), 1 mM EDTA, 2 μg/ml

417 aprotinin, 10 μg/ml leupeptin, 1 mM PMSF, 1:100 (vol/vol) Phosphatase Inhibitor Cocktail 2,

418 1:100 Phosphatase Inhibitor Cocktail 3, 10 mM NaF, and 20 μM PUGNAc) for each ~50 mg

419 portion of wet-weight tissue. Lysates were reduced with 5mM DTT, alkylated with 10 mM IAM,

420 and digestion performed in solution with 1 mAU LysC per 50 μg of total protein and trypsin at an

421 enzyme/substrate ratio of 1:49. Reactions were quenched with FA and brought to pH = 3 with

422 FA. Peptides were desalted on 200 mg tC18 SepPak cartridges and dried by vacuum

423 centrifugation. 340 μg of peptides were labeled with 10-plex Tandem Mass Tag reagents

424 (TMT10, Fisher Scientific), according to manufacturer's instructions. To enable quantification of

425 peptides across all 12 samples, the samples were labeled in sets of 10 across two different

426 TMT10 pools in a crossover design with 8 of 12 samples analyzed in both TMT10 pools. A

427 50/50 mix of both AALE vector control lysates was used as an internal reference in both TMT10

428 runs (**Supplementary Fig. 1b**).

18

429

430   Each TMT10-plex was desalted in a 200 mg tC18 SepPak cartridge and fractionated using

431   offline HPLC. 5% of each fraction was collected into an HPLC vial for proteome analysis by LC-

432   MS/MS. The remaining 95% was processed for phospho-peptide enrichment via immobilized

433   metal affinity chromatography (IMAC). IMAC enrichment was performed using Ni-NTA

434   Superflow Agarose beads incubated with peptides solubilized in a final concentration of 80%

435   MeCN/0.1% TFA. Phospho-enriched peptides were desalted and collected into an HPLC vial for

436   analysis by LC-MS/MS.

437

438   Online fractionation was performed using a nanoflow Proxeon EASY-nLC 1200 UHPLC system

439   (Thermo Fisher Scientific) and separated peptides were analyzed on a benchtop Orbitrap Q

440   Exactive Plus mass spectrometer (Thermo Fisher Scientific) equipped with a nanoflow

441   ionization source (James A. Hill Instrument Services, Arlington, MA). In-house packed columns

442   (20 cm x 75 μm diameter C18 silica picofrit capillary column; 1.9 μm ReprosIl-Pur C18-AQ

443   beads, Dr. Maisch GmbH, r119.aq; Picofrit 10 μm tip opening, New Objective, PF360-75-10-N-

444   5). Mobile phase flow rate was 200 nL/min, comprised of 3 % acetonitrile/0.1 % formic acid

445   (Solvent A) and 90 % acetonitrile /0.1 % formic acid (Solvent B). The 110 min LC-MS/MS

446   method consisted of a 10 min column-equilibration procedure; a 20 min sample-loading

447   procedure; and the following gradient profile: (min: % B) 0:2; 2:6; 85:30; 94:60; 95:90; 100:90;

448   101:50; 110:50 (the last two steps at 500 nL/min flow rate). Data-dependent acquisition was

449   performed using Xcalibur QExactive v2.4 software in positive ion mode at a spray voltage of

450   2.00 kV. MS1 Spectra were measured with a resolution of 70,000, an AGC target of 3e6 and a

451   mass range from 300 to 1800 m/z. Up to 12 MS/MS spectra per duty cycle were triggered at a

452   resolution of 35,000, an AGC target of 5e4, an isolation window of 0.7 m/z, a maximum ion time

453   of 120 msec, and normalized collision energy of 30. Peptides that triggered MS/MS scans were

454   dynamically excluded from further MS/MS scans for 20 sec. Charge state screening was

455   enabled to reject precursor charge states that were unassigned, 1, or >6. Peptide match was

456   set to preferred for monoisotopic precursor mass assignment.

457

458   **Protein-peptide identification, phosphosite localization, and quantification**

459   MS data was interpreted using the Spectrum Mill software package v6.0 pre-release (Agilent

460   Technologies, Santa Clara, CA. MS/MS spectra were merged if they were acquired within +/- 45

461   sec of each other with the same precursor m/z. Also, MS/MS spectra that did not have a

462   sequence tag length > 0 (i.e., minimum of two masses separated by the in chain mass of an

463   amino acid) or did not have a precursor MH+ in the range of 750-6000 were excluded from

464   searching. MS/MS spectra searches were performed against a concatenated UniProt human

465   reference proteome sequence database containing 58,929 human proteins including isoforms

466   (obtained 10/17/2014) and 150 additional common laboratory contaminants. ESI-QEXACTIVE-

467   HCD-3 scoring parameters were used for both whole proteome and phosphoproteome datasets.

468   Spectra were allowed +/- 20 ppm mass tolerance for precursor as well as product ions, 30%

469   minimum matched peak intensity, and "trypsin allow P" was set as enzyme specificity with up to

470   4 missed cleavages allowed. Carbamidomethylation at cysteine was set as fixed modification

471   together with TMT10 isobaric labels at lysine residues (N-termini would be considered

472   regardless if it was TMT labelled). Acetylation of protein N-termini andoxidized methionine were

473   set as variable modifications with a precursor MH+ shift range of -18 to 64 Da for the proteome

474   searches. For the phosphoproteome searches the precursor MH+ shift range was set to 0 to

475   272 Da and variable modifications of phosphorylation of serine, threonine, and tyrosine.

476   Identities interpreted for individual spectra were automatically designated as confidently

477   assigned using the Spectrum Mill autovalidation module to use target-decoy based false

478   discovery rate (FDR) estimates to apply score threshold criteria. For the whole proteome

479   datasets, thresholding was done at the spectral (< 1.2%) and protein levels (< 0.1%) . For the

480   phosphoproteome datasets, thresholding was done at the spectral (< 1.2%) and phosphosite

481   levels (< 1.0%).

482   Replicates across TMT-plexes were highly correlated (**Supplementary Fig. 1c)** with median

483   Pearson r = 0.87 and 0.69 for proteome and phosphoproteome, respectively**.** Technical

484   replicates and biological replicates were merged to generate final total proteome and phospho-

485   proteome profiles for each isogenic cell line (**Supplementary Tables 1 and 2**). Replicate-level

486   profiles are also supplied as JavaScript Object Notation (.json) files that can be visualized and

487   analyzed using the Morpheus Matrix Visualization and Analysis Software at

488   https://software.broadinstitute.org/morpheus (**Supplementary Files 1 and 2**). Differential

489   protein and phospho-site signatures were generated by computing the mean $\log_2$(fold change)

490   of the abundance of each site in each sample compared to the vector control cells. Statistical

491   significance of differentially abundant proteins and phosphosites was determined by performing

492   a one sample moderated t-test with multiple hypothesis correction (**Supplementary Tables 1**

493   **and 2**).

494

495   **Integrative Analysis**

496   Correlation of changes in protein expression and changes in RNA expression was modeled

497   using R's lm() function. 95% prediction intervals were calculated to determine genes with weak

498   concordance between protein and RNA expression.

499

500   **Gene Set Enrichment Analysis**

501   Analysis of enrichment of KRAS signaling in differential RNA expression profiles was performed

502   in R with the goseq package[56]. KRAS signaling gene sets were taken from MSigDB hallmark

503   gene sets[22,57].

504

Transcription Factor Target Enrichment Analysis

506   Analysis of over-representation of Transcription Factor targets was performed with ChEA3 by

507   submitting lists of differentially expressed genes (|LFC| > 1 and FDR < 0.05). ChEA3 performs

508   Fisher's Exact Test to compare the input gene set to TF target gene sets in six different

509   libraries[58]. Analysis of the Enrichr Queries library was selected as the focus of the present

510   study. Transcription factors resulting from this analysis were annotated as one of four groups of

511   EMT association. These four groups were the Snail gene family, confirmed EMT genes defined

512   by dbEMT[59], genes shown to be associated with EMT in at least one study in literature, and

513   genes unrelated to EMT.

514

Antibodies and immunoblotting

516   Antibodies against FOSL1 (D80B4), TXNIP (D5F3E), and Vimentin (D21H3) were purchased

517   from Cell Signaling Technology. Vinculin (V9264) was purchased from Sigma Aldrich.

518   Secondary antibodies StarBright Blue 700 Goat anti-Rabbit IgG, StarBright Blue 520 Goat anti-

519   Rabbit IgG and StarBright Blue 520 Goat anti-Mouse IgG (12005867) were purchased from Bio-

520   Rad. Antibody against RIT1 (#53720) was purchased from Abcam. Cell lysates were prepared

521   in RTK lysis buffer with protease (11836153001, Roche) and phosphatase (04906837001,

522   Roche) inhibitors added and quantified by the BCA assay (Thermo Scientific Waltham, MA).

523   Samples were then boiled in Laemmli buffer (1610747, Bio-Rad, Hercules, CA) and 50 ug of

524   protein was loaded onto 4-15% Mini-Protean TGX (4561084, Bio-Rad, Hercules, CA) gels.

525   Protein gels were run and transferred to PVDF membranes (1704274, Bio-Rad, Hercules, CA)

526   according to manufacturer's instructions. Proteins were detected by specific primary antibody

527   and secondary antibody then visualized using the ChemiDoc MP Imaging System (Bio-Rad,

528   Hercules, CA).

529

530

KSEA analysis

Kinase-substrate enrichment analysis (KSEA)[60] was performed using the KSEA App[34] (https://casecpb.shinyapps.io/ksea/) using kinase-substrate mappings from PhosphoSitePlus[35] and a p value threshold of < 0.05. A minimum of five detected phospho-site substrates were needed for kinases to be included in the analysis. The full list of kinase scores and number of substrates are shown in Supplementary Table 5. 36 kinases had sufficient substrate sites detected to be included in the analysis. Kinase-substrate mappings are shown in Supplementary Table 5.

DATA AVAILABILITY

The RNA-seq data have been deposited in the NCBI Gene Expression Omnibus database with accession number GSE146479. All mass spectra contributing to this study can be downloaded in the original instrument vendor format from the MassIVE online repository (Accession number to be updated prior to publication.)

554

AUTHOR CONTRIBUTIONS

556   A.H.B. conceived of and directed the study. S.C. and P.M. supervised the LC-MS/MS

557   experiments. F.M. performed the proteomics data analysis, with contributions from

558   A.H.B. and K.H. A.L. performed the transcriptome analysis. A.L. and A.H.B. wrote the

559   manuscript. A.L., K.H., S.M., I.F., S.F., J.W., and A.H.B. performed experiments. All

560   authors discussed results and provided input on the manuscript.

561

562

563
564

Figure Legends

Figure 1. Comparative multi-omic profiling of KRAS- and RIT1-mutant human lung epithelial cells. a, Protein alignment of KRAS-4B (Uniprot #P01116-2) and RIT1 Isoform 1 (Uniprot #Q92963-1) generated by ClustalW2[61]. Stars indicate the position of the RIT1^{M90I} or KRAS^{G12V} and KRAS^{Q61} variants used in this study. Asterisks indicate fully conserved residues. Colons indicate strongly conserved residues. Periods indicate weakly conserved residues. **b,** Soft agar colony formation assay of isogenic AALE human lung epithelial cells. **, $p < 0.01$; ****, $p<0.0001$ by two-tailed t-test. **c,** Western blot using anti-RAS and anti-RIT1 antibodies (top panels), or antibodies against phosphorylated ERK1/2 or vinculin (loading control). SE = short exposure, LE = long exposure. Isogenic AALE cells were cultured in the presence or absence of EGF for 12 hours. **d,** LC-MS/MS workflow for generation of proteome and phosphoproteome profiles. bRP, basic reverse phase chromatography. IMAC, immobilized metal affinity chromatography. **e,** Workflow for Illumina RNA-seq analysis. **f,** mRNA quantification in transcripts per million (TPM) showing mean ± SD of RIT1 (left) or KRAS (right) in isogenic AALE cells, n = 3 per cell line. *, $p < 0.05$; ****, $p < 0.0001$ by two-tailed Student's t-test compared to vector control cells. **g,** RNA-seq quantification of variant allele expression. Data shown is the percentage of reads at the M90I, G12V, or Q61H variant site for the variant allele or wild-type allele.

Figure 2. Quantitative proteome and transcriptome profiling identifies similarity in RIT1^{M90I}-mutant and KRAS-mutant signaling networks. a, Volcano plots of global proteome data from isogenic AALE cells showing the log$_2$(fold change) ("LFC") in protein abundance in each cell line compared to vector control cells. The y-axis displays the negative log$_{10}$(p value) calculated from a one sample moderated t-test with multiple hypothesis correction by the Benjamini-Hochberg method. **b,** Western blot validation of FOSL1 increased protein abundance in RIT1- and KRAS-mutant cells. The chart shows the LFC of FOSL1 as determined by LC-

25

590   MS/MS. Western blot below shows FOSL1 abundance or Vinculin (loading control). **c**, Western

591   blot validation of TXNIP protein abundance in RIT1- and KRAS-mutant cells. The chart shows

592   the LFC of TXNIP as determined by LC-MS/MS. **d,** Correlation heatmap showing pairwise

593   Pearson and Spearman correlations of each proteome and phosphoproteome replicate to every

594   other replicate. To enable correlation of proteome with phosphoproteome, phosphosites were

595   collapsed to the protein level by taking the median of all phosphosites for each protein. **e,**

596   Principal component analysis (PCA) of RNA-seq data. Circles correspond to control vector or

597   wild-type replicates. Diamonds correspond to RIT1- or KRAS-mutant profiles.

598   **Figure 3. RIT1^{M90I} promotes epithelial-to-mesenchymal (EMT) transition. a,** Gene set

599   overlap analysis of up-regulated ("Up"; LFC>2) and down-regulated ("down"; LFC<-2) proteins

600   using MSigDB Hallmark Pathways[22]. "K" and "R" indicate analysis based on mean LFC of

601   KRAS^{G12V}/KRAS^{Q61H} cells or RIT1^{WT}/RIT1^{M90I} cells, respectively. Circle size corresponds to the *p*

602   value of gene set overlap analysis determined by MSigDB. **b**, LFC of protein abundance of EMT

603   marker genes as determined by LC-MS/MS, relative to vector control cells. **c,** Transcription

604   factor target enrichment analysis of differentially expressed genes in RIT1^{M90I}-mutant cells using

605   Enrichr libraries. FET, Fisher's exact test. Red = Snail family. Orange = confirmed EMT genes in

606   dbEMT[59]. Pale orange = EMT-associated genes in literature. **d,** Enrichr analysis of KRAS^{G12V}-

607   mutant proteome data. Annotation is the same as in **c**.

608   **Figure 4. RIT1- and KRAS-mutant cells suppress Class I MHC expression via global loss**

609   **of antigen processing and presenting machinery. a**, Rank plot of all protein abundance

610   changes in KRAS^{G12V}-mutant cells compared to vector control, generated by LC-MS/MS. HLA-

611   A,-B,-C, and -F proteins are labeled in blue. **b,** Heat map showing HLA protein abundance in

612   each global proteome replicate. Replicates were clustered by unsupervised hierarchical

613   clustering using all detected proteins. **c,** Protein abundance of B2M in LC-MS/MS data. **d,** Top

614   differentially abundant proteins between RIT1^{WT} cells and all other cell lines. Proteins are

615   ranked by the signal-to-noise (S2N) statistic, shown in the bar chart at the right. **e**, StringDB[62]

616   network analysis of proteins with S2N>2.5 in analysis shown in **d**. The network was significantly

617   more connected than expected by chance (p < 1e-16). Disconnected nodes, single connected

618   nodes, and disconnected clusters have been removed from the visualization. Edges represent

619   high confidence interaction scores (>0.9) and network edge thickness indicates the strength of

620   data support from all StringDB active interaction sources. **f,** Protein abundance of PSMB9 in LC-

621   MS/MS data. **g,** Global proteome-transcriptome correlation analysis. A dashed diagonal line

622   displays the linear regression generated by comparing the LFC of each gene in the

623   transcriptome to its respective protein LFC in the proteome. The resulting Pearson correlation

624   coefficient (r) is shown. Genes outside the 95% prediction interval are plotted in red, and include

625   HLA genes, metallothioneins, and intermediate filament proteins Vimentin (VIM) and alpha

626   internexin (INA).

627   **Figure 5. Phosphoproteomic profiling illuminates novel differential post-translational**

628   **modifications in RIT1^{M90I}- and KRAS-mutant cells. a,** KSEA analysis of AALE

629   phosphoproteomes. Top differentially phosphorylated kinase substrates are shown. The full

630   KSEA results are shown in **Supplementary Fig 4b-c. b**, Violin plot of phospho-site abundance

631   of phospho-sites that are RPS6KA1 substrates. **c,** Violin plot of phospho-site abundance of

632   phospho-sites that are MAPKAPK2 substrates. **d,** Marker selection analysis identifies

633   differentially phosphorylated sites in KRAS-mutant cells compared to RIT1-mutant cells.

634   Phosphosites from KRAS-mutant and RIT1^{M90I}-mutant replicate-level phosphoproteome profiles

635   (**Supplementary File 2**) were compared by two-tailed t-test. The top 20 significantly (FDR <

636   0.05) differentially phosphorylated sites in each direction are shown and ranked by t-statistic. A

637   heat map displays the LFC in phosphorylated peptide abundance of each site compared to

638   vector control, after normalizing to total protein abundance. **e,** LFC of EGFR phosphosites in

639 KRAS-mutant and RIT1-mutant cells. Data shown is the mean + SD of n=8 KRAS-mutant

640 replicates and n=4 RIT1-mutant replicates. *, FDR < 0.01 as determined by two-tailed t-test and

641 two-stage linear step-up procedure of Benjamini, Krieger and Yekutieli. **f,** Relative

642 phosphorylation of USO1 at serine 48 as determined by LC-MS/MS. Box and whiskers show the

643 25th-75th percentiles and minimum to maximum of the data, respectively. **g,** Relationship of

644 USO1 S48 phosphorylation to KRAS total protein abundance. A dashed line displays the linear

645 regression fit and gray lines display the 95% confidence interval of the linear model. *r* = 0.70, *p*

646 < 0.01.

647

648 **SUPPLEMENTARY FIGURE LEGENDS**

649 **Supplementary Figure 1. Workflow and quality control of proteomic and transcriptomic**

650 **profiling. a,** Replicate-level workflow for tandem mass tag (TMT) labeling and LC-MS/MS.

651 Lysates from duplicate sets of six isogenic cell lines were used to generate two TMT-plex sets,

652 with control samples used to link the two sets. **b,** TMT 10-plex layout showing mass tags

653 associated with each replicate. **c,** Average pairwise replicate correlations (Pearson *r*) of all

654 replicates from each sample group indicated. **d,** Enrichment analysis of differentially expressed

655 genes between KRAS or RIT1 perturbed lines and vector controls using *goseq*[56]. mSigDB

656 hallmark gene sets specific to KRAS signaling are shown. **e,** RNA-seq run and mapping

657 statistics show total reads, mapped reads, and reads mapped to rRNA, for each sample.

658

659 **Supplementary Figure 2. RIT1 and KRAS promote epithelial-to-mesenchymal transition.**

660 **a,** Changes in mRNA transcript levels of EMT genes *VIM*, *CDH2*, *FN1*, and *KRT19*, in each

661 isogenic cell line compared to vector control. LFC, $\log_2$(fold-change) compared to vector cells. **b,**

662 Transcription factor target enrichment analysis using Enrichr libraries of differentially expressed

663 genes in RIT1[WT], KRAS[WT], and KRAS[Q61H]-mutant cells. FET, Fisher's exact test. Red = Snail

664 family. Orange = confirmed EMT genes in dbEMT[59]. Pale orange = EMT-associated genes in

665 literature.

666

667 **Supplementary Figure 3. Post-transcriptional loss of Class I MHC proteins. a,** Rank plot of

668 all protein abundance changes in KRAS^{Q61H}-mutant or RIT1^{M90I}-mutant cells compared to vector

669 control, generated by LC-MS/MS. HLA-A,-B,-C, and -F proteins are labeled. LFC, log$_2$ fold-

670 change. **b,** Change in mRNA transcript levels of HLA genes and upstream regulators of MHC

671 Class I, in each isogenic cell line compared to vector controls. LFC, log$_2$ fold change compared

672 to vector cells. **c,** Correlation of protein levels in HLA-A and PSMB9 across each isogenic cell

673 line. A line is the best-fit linear regression with significant non-zero slope ($p < 0.05$).

674

675 **Supplementary Figure 4. Phosphoproteome profiling identifies enhanced**

676 **phosphorylation of specific kinase substrates in KRAS- and RIT1-mutant cells. a,** Pairwise

677 replicate correlation (Pearson r) heatmap and unsupervised clustering of phosphoproteome

678 data. **b,** KSEA of phosphoproteome data for RIT1^{WT} and RIT1^{M90I}-expressing cells. The kinase

679 z-score indicates the overall score for each kinase listed, normalized by the total number of

680 substrates. Significant scores ($p<0.05$) are indicated in red and blue. Phospho-sites of kinases

681 in red were more highly abundant in the cell line compared to vector control, whereas phospho-

682 sites of kinases in blue were more highly abundant in vector control than the indicated cell line.

683 **c,** KSEA of phosphoproteome data for KRAS-expressing cells. Labeling as in (**b**). **d,** Violin plot

684 of phospho-site abundance of AKT1 substrate sites. **e,** Violin plot of phospho-site abundance of

685 PRKCA substrate sites. **f**, Violin plot of phospho-site abundance of AURKB substrate sites. **g,**

686 EGFR protein abundance in LC-MS/MS data compared to vector control. **f,** Proportion of

687 phosphorylated sites in AHNAK proteins with differential phosphorylation between KRAS-mutant

688 and RIT1^{M90I}-mutant cells. Data shown is the percentage of differentially abundant

29

689   phosphorylation sites in AHNAK and AHNAK2 compared to all other sites. Significance was

690   determined from the analysis in (**b**), FDR < 0.05. ****, $p < 0.0001$ by two-sided Fisher's exact

691   test.

692

693 **References**

694

695   1.   Trahey, M. & McCormick, F. A cytoplasmic protein stimulates normal N-ras p21 GTPase,

696   but does not affect oncogenic mutants. *Science* **238**, 542–545 (1987).

697   2.   Emil F. Pai, Wolfgang Kabsch, Ute Krengel, Kenneth C. Holmes, Jacob John & Alfred

698   Wittinghofer. Structure of the guanine-nucleotide-binding domain of the Ha-ras oncogene

699   p21 in the triphosphate conformation. *Nature* **2**, 1105–1111 (1989).

700   3.   Nakano, H. *et al.* Isolation of transforming sequences of two human lung carcinomas:

701   structural and functional analysis of the activated c-K-ras oncogenes. *Proc. Natl. Acad. Sci.*

702   *U. S. A.* **81**, 71–75 (1984).

703   4.   Rodenhuis, S. *et al.* Mutational activation of the K-ras oncogene. A possible pathogenetic

704   factor in adenocarcinoma of the lung. *N. Engl. J. Med.* **317**, 929–935 (1987).

705   5.   Berger, A. H. *et al.* Oncogenic RIT1 mutations in lung adenocarcinoma. *Oncogene* **33**,

706   4418–4423 (2014).

707   6.   Gómez-Seguí, I. *et al.* Novel recurrent mutations in the RAS-like GTP-binding gene RIT1 in

708   myeloid malignancies. *Leukemia* **27**, 1943–1946 (2013).

709   7.   Aoki, Y. *et al.* Gain-of-Function Mutations in RIT1 Cause Noonan Syndrome, a RAS/MAPK

710   Pathway Syndrome. *Am. J. Hum. Genet.* **93**, 173–180 (2013).

711   8.   Cai, W. *et al.* Rit GTPase signaling promotes immature hippocampal neuronal survival. *J.*

712   *Neurosci.* **32**, 9887–9897 (2012).

713   9.   Rusyn, E. V. *et al.* Rit, a non-lipid-modiÆed Ras-related protein, transforms NIH3T3 cells

714   without activating the ERK, JNK, p38 MAPK or PI3K/Akt pathways. *Oncogene* **19**, 4685–

715   4694 (2000).

716   10. Sakabe, K. *et al.* Potent transforming activity of the small GTP-binding protein Rit in NIH

717   3T3 cells: evidence for a role of a p38gamma-dependent signaling pathway. *FEBS Lett.*

718   **511**, 15–20 (2002).

719 11. Castel, P. *et al.* RIT1 oncoproteins escape LZTR1-mediated proteolysis. *Science* **363**,

720   1226–1230 (2019).

721 12. Fang, Z. *et al.* Biochemical Classification of Disease-associated Mutants of RAS-like

722   Protein Expressed in Many Tissues (RIT1). *J. Biol. Chem.* **291**, 15641–15652 (2016).

723 13. Lundberg, A. S. *et al.* Immortalization and transformation of primary human airway epithelial

724   cells by gene transfer. *Oncogene* **21**, 4577–4586 (2002).

725 14. Simanshu, D. K., Nissley, D. V. & McCormick, F. RAS Proteins and Their Regulators in

726   Human Disease. *Cell* **170**, 17–33 (2017).

727 15. Young, M. R. & Colburn, N. H. Fra-1 a target for cancer prevention or intervention. *Gene*

728   **379**, 1–11 (2006).

729 16. Mechta, F., Lallemand, D., Pfarr, C. M. & Yaniv, M. Transformation by ras modifies AP1

730   composition and activity. *Oncogene* **14**, 837–847 (1997).

731 17. Casalino, L., De Cesare, D. & Verde, P. Accumulation of Fra-1 in ras-transformed cells

732   depends on both transcriptional autoregulation and MEK-dependent posttranslational

733   stabilization. *Mol. Cell. Biol.* **23**, 4401–4415 (2003).

734 18. Yoshihara, E. *et al.* Thioredoxin/Txnip: redoxisome, as a redox switch for the pathogenesis

735   of diseases. *Front. Immunol.* **4**, 514 (2014).

736 19. Parikh, H. *et al.* TXNIP regulates peripheral glucose metabolism in humans. *PLoS Med.* **4**,

737   e158 (2007).

738 20. Elgort, M. G., O'Shea, J. M., Jiang, Y. & Ayer, D. E. Transcriptional and Translational

739   Downregulation of Thioredoxin Interacting Protein Is Required for Metabolic

740   Reprogramming during G(1). *Genes Cancer* **1**, 893–907 (2010).

741 21. Ye, Z. & Ayer, D. E. Ras Suppresses TXNIP Expression by Restricting Ribosome

742   Translocation. *Mol. Cell. Biol.* **38**, (2018).

743 22. Liberzon, A. *et al.* The Molecular Signatures Database (MSigDB) hallmark gene set

744   collection. *Cell Syst* **1**, 417–425 (2015).

745   23. Ye, X. & Weinberg, R. A. Epithelial-Mesenchymal Plasticity: A Central Regulator of Cancer

746   Progression. *Trends Cell Biol.* **25**, 675–686 (2015).

747   24. Singh, A. *et al.* A gene expression signature associated with 'K-Ras addiction' reveals

748   regulators of EMT and tumor cell survival. *Cancer Cell* **15**, 489–500 (2009).

749   25. Shao, D. D. *et al.* KRAS and YAP1 converge to regulate EMT and tumor survival. *Cell* **158**,

750   171–184 (2014).

751   26. Shukla, S. A. *et al.* Comprehensive analysis of cancer-associated somatic mutations in

752   class I HLA genes. *Nat. Biotechnol.* **33**, 1152–1158 (2015).

753   27. Conway, J. R., Kofman, E., Mo, S. S., Elmarakeby, H. & Van Allen, E. Genomics of

754   response to immune checkpoint therapies for cancer: implications for precision medicine.

755   *Genome Med.* **10**, 93 (2018).

756   28. Gettinger, S. *et al.* Impaired HLA Class I Antigen Processing and Presentation as a

757   Mechanism of Acquired Resistance to Immune Checkpoint Inhibitors in Lung Cancer.

758   *Cancer Discov.* **7**, 1420–1435 (2017).

759   29. Jongsma, M. L. M., Guarda, G. & Spaapen, R. M. The regulatory network behind MHC

760   class I expression. *Mol. Immunol.* **113**, 16–21 (2019).

761   30. Burr, M. L. *et al.* An Evolutionarily Conserved Function of Polycomb Silences the MHC

762   Class I Antigen Presentation Pathway and Enables Immune Evasion in Cancer. *Cancer*

763   *Cell* **36**, 385–401.e8 (2019).

764   31. Seliger, B. *et al.* Down-regulation of the MHC class I antigen-processing machinery after

765   oncogenic transformation of murine fibroblasts. *Eur. J. Immunol.* **28**, 122–133 (1998).

766   32. Roux, P. P. *et al.* RAS/ERK signaling promotes site-specific ribosomal protein S6

767   phosphorylation via RSK and stimulates cap-dependent translation. *J. Biol. Chem.* **282**,
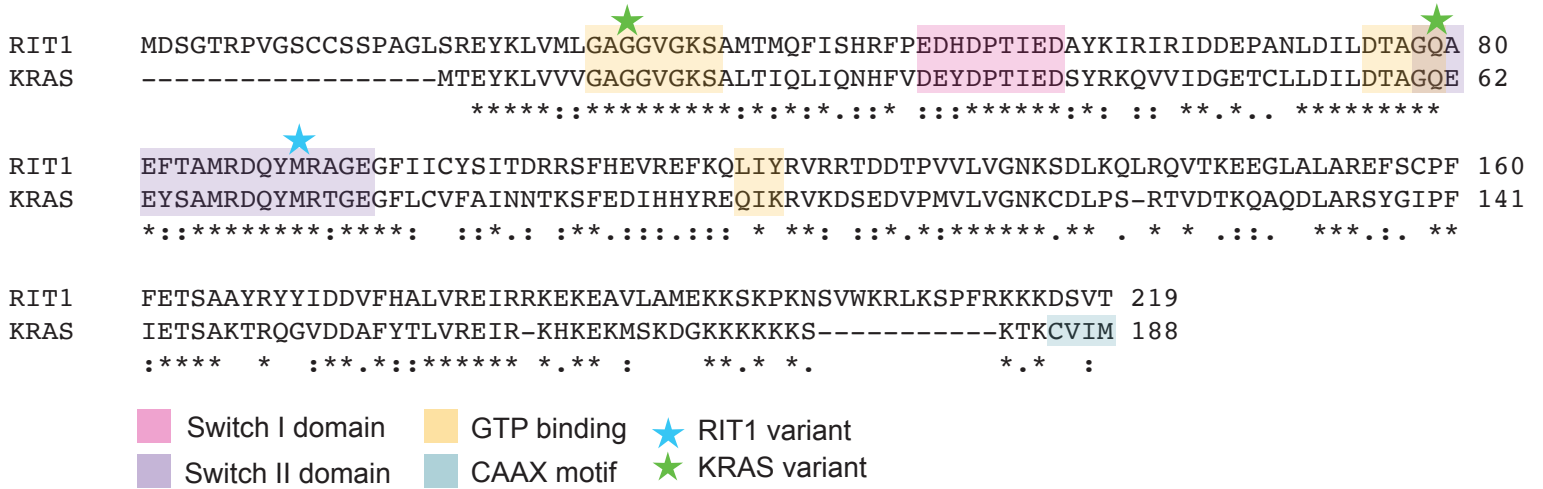
768   14056–14064 (2007).

769   33. Mendoza, M. C., Er, E. E. & Blenis, J. The Ras-ERK and PI3K-mTOR pathways: cross-talk

770   and compensation. *Trends Biochem. Sci.* **36**, 320–328 (2011).

771   34. Wiredja, D. D., Koyutürk, M. & Chance, M. R. The KSEA App: a web-based tool for kinase

772   activity inference from quantitative phosphoproteomics. *Bioinformatics* (2017)

773   doi:10.1093/bioinformatics/btx415.

774   35. Hornbeck, P. V. *et al.* PhosphoSitePlus: a comprehensive resource for investigating the

775   structure and function of experimentally determined post-translational modifications in man

776   and mouse. *Nucleic Acids Res.* **40**, D261–D270 (2011).

777   36. Linding, R. *et al.* Systematic discovery of in vivo phosphorylation networks. *Cell* **129**, 1415–

778   1426 (2007).

779   37. Unni, A. M., Lockwood, W. W., Zejnullahu, K., Lee-Lin, S.-Q. & Varmus, H. Evidence that

780   synthetic lethality underlies the mutual exclusivity of oncogenic KRAS and EGFR mutations

781   in lung adenocarcinoma. *Elife* **4**, e06907 (2015).

782   38. Chang, C. P. *et al.* Ligand-induced internalization of the epidermal growth factor receptor is

783   mediated by multiple endocytic codes analogous to the tyrosine motif found in constitutively

784   internalized receptors. *J. Biol. Chem.* **268**, 19312–19320 (1993).

785   39. Tong, J., Taylor, P., Peterman, S. M., Prakash, A. & Moran, M. F. Epidermal growth factor

786   receptor phosphorylation sites Ser991 and Tyr998 are implicated in the regulation of

787   receptor endocytosis and phosphorylations at Ser1039 and Thr1041. *Mol. Cell. Proteomics*

788   **8**, 2131–2144 (2009).

789   40. Yu, I.-M. & Hughson, F. M. Tethering factors as organizers of intracellular vesicular traffic.

790   *Annu. Rev. Cell Dev. Biol.* **26**, 137–156 (2010).

791   41. Prior, I. A. & Hancock, J. F. Ras trafficking, localization and compartmentalized signalling.

792   *Semin. Cell Dev. Biol.* **23**, 145–153 (2012).

793   42. Shao, H., Kadono-Okuda, K., Finlin, B. S. & Andres, D. A. Biochemical characterization of

794 the Ras-related GTPases Rit and Rin. *Arch. Biochem. Biophys.* **371**, 207–219 (1999).

795 43. Park, J. W. *et al.* AHNAK Loss in Mice Promotes Type II Pneumocyte Hyperplasia and

796 Lung Tumor Development. *Mol. Cancer Res.* **16**, 1287–1298 (2018).

797 44. Lee, I. H. *et al.* Ahnak functions as a tumor suppressor via modulation of TGFβ/Smad

798 signaling pathway. *Oncogene* **33**, 4675–4684 (2014).

799 45. Che, Y. *et al.* KRAS regulation by small non-coding RNAs and SNARE proteins. *Nat.*

800 *Commun.* **10**, 5118 (2019).

801 46. Ritchie, C. *et al.* Analysis of K-Ras Interactions by Biotin Ligase Tagging. *Cancer Genomics*

802 *Proteomics* **14**, 225–239 (2017).

803 47. Ambrogio, C. *et al.* KRAS Dimerization Impacts MEK Inhibitor Sensitivity and Oncogenic

804 Activity of Mutant KRAS. *Cell* **172**, 857–868.e15 (2018).

805 48. Pylayeva-Gupta, Y., Grabocka, E. & Bar-Sagi, D. RAS oncogenes: weaving a tumorigenic

806 web. *Nat. Rev. Cancer* **11**, 761–774 (2011).

807 49. Carpenter, A. E. *et al.* CellProfiler: image analysis software for identifying and quantifying

808 cell phenotypes. *Genome Biol.* **7**, R100 (2006).

809 50. Dobin, A. *et al.* STAR: ultrafast universal RNA-seq aligner. *Bioinformatics* **29**, 15–21 (2013).

810 51. Picard Tools - By Broad Institute. http://broadinstitute.github.io/picard.

811 52. Wang, L., Wang, S. & Li, W. RSeQC: quality control of RNA-seq experiments.

812 *Bioinformatics* **28**, 2184–2185 (2012).

813 53. Liao, Y., Smyth, G. K. & Shi, W. FeatureCounts: An efficient general purpose program for

814 assigning sequence reads to genomic features. *Bioinformatics* **30**, 923–930 (2014).

815 54. Robinson, M. D., McCarthy, D. J. & Smyth, G. K. edgeR: A Bioconductor package for

816 differential expression analysis of digital gene expression data. *Bioinformatics* **26**, 139–140

817 (2009).

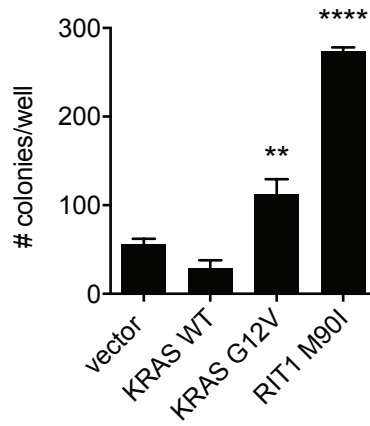818 55. Mertins, P. *et al.* Reproducible workflow for multiplexed deep-scale proteome and

819   phosphoproteome analysis of tumor tissues by liquid chromatography-mass spectrometry.

820   *Nat. Protoc.* **13**, 1632–1661 (2018).

821   56. Young, M. D., Wakefield, M. J., Smyth, G. K. & Oshlack, A. Gene ontology analysis for

822   RNA-seq: accounting for selection bias. *Genome Biol.* **11**, R14 (2010).

823   57. Subramanian, A. *et al.* Gene set enrichment analysis: a knowledge-based approach for

824   interpreting genome-wide expression profiles. *Proc. Natl. Acad. Sci. U. S. A.* **102**, 15545–

825   15550 (2005).

826   58. Keenan, A. B. *et al.* ChEA3: transcription factor enrichment analysis by orthogonal omics

827   integration. *Nucleic Acids Res.* **47**, W212–W224 (2019).

828   59. Zhao, M., Liu, Y., Zheng, C. & Qu, H. dbEMT 2.0: An updated database for epithelial-

829   mesenchymal transition genes with experimentally verified information and precalculated

830   regulation information for cancer metastasis. *J. Genet. Genomics* **46**, 595–597 (2019).

831   60. Casado, P. *et al.* Kinase-substrate enrichment analysis provides insights into the

832   heterogeneity of signaling pathway activation in leukemia cells. *Sci. Signal.* **6**, rs6 (2013).

833   61. Larkin, M. A. *et al.* Clustal W and Clustal X version 2.0. *Bioinformatics* **23**, 2947–2948

834   (2007).

835   62. Szklarczyk, D. *et al.* STRING v10: protein-protein interaction networks, integrated over the

836   tree of life. *Nucleic Acids Res.* **43**, D447–52 (2015).
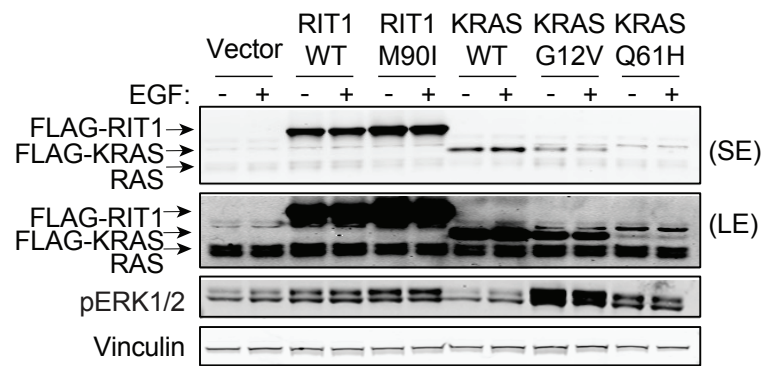
837
838
839
840
841
842
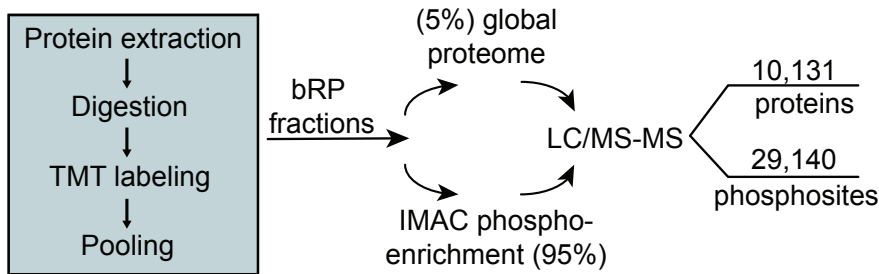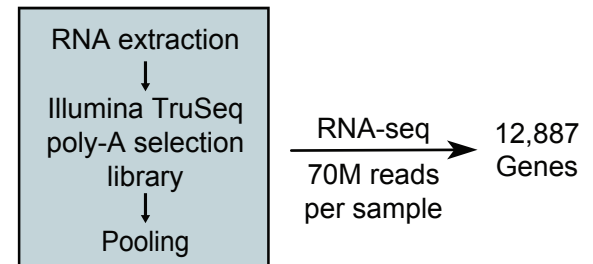843
844

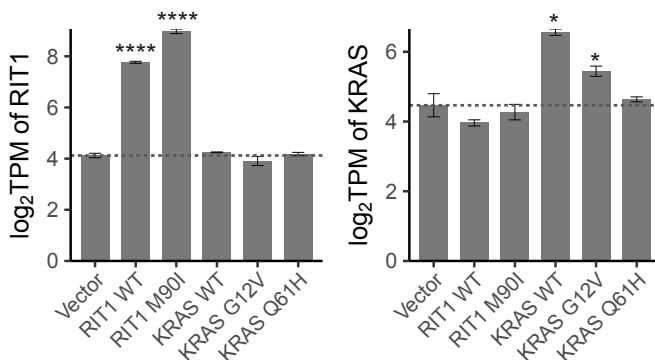**Figure 1**

a

```
RIT1    MDSGTRPVGSCCSSPAGLSREYKLVMLGAGGVGKSAMTMQFISHRFPEDHDPTIEDAYKIRIRIDDEPANLDILDTAGQA  80
KRAS    -----------------MTEYKLVVVGAGGVGKSALTIQLIQNHFVDEYDPTIEDSYRKQVVIDGETCLLDILDTAGQE  62
                         *****::*********:*:*:*.::*  ::::*****:*: :: **.*.. ********

RIT1    EFTAMRDQYMRAGEGFIICYSITDRRSFHEVREFKQLIYRVRRTDDTPVVLVGNKSDLKQLRQVTKEEGLALAREFSCPF  160
KRAS    EYSAMRDQYMRTGEGFLCVFAINNTKSFEDIHHYREQIKRVKDSEDVPMVLVGNKCDLPS-RTVDTKQAQDLARSYGIPF  141
                *::*******:*****:  ::*.: :**.::::.::* * **: ::*.*:*****.** . * * .::.  ***.:. **

RIT1    FETSAAYRYYIDDVFHALVREIRRKEKEAVLAMEKKSKPKNSVWKRLKSPFRKKKDSVT  219
KRAS    IETSAKTRQGVDDAFYTLVREIR-KHKEKMSKDGKKKKKKS----------KTKCVIM  188
               :**** *  :**.*::****** *.** :    **.* *.           *.* :
```

Switch I domain   GTP binding   ★ RIT1 variant
Switch II domain   CAAX motif   ★ KRAS variant

b

c

d

e

f

g

Figure 2

Figure 3

Figure 4

Figure 5

a KSEA score — RIT1 WT, RIT1 M90I, KRAS WT, KRAS Q61H, KRAS G12V; RPS6KA1, AKT1, MAPKAPK2, AURKB

b RPS6KA1 substrates — substrate p-site LFC; RIT1 WT, RIT1 M90I, KRAS WT, KRAS G12V, KRAS Q61H

c MAPKAPK2 substrates — substrate p-site LFC; RIT1 WT, RIT1 M90I, KRAS WT, KRAS G12V, KRAS Q61H

d KRAS G12V, KRAS Q61H, RIT1 M90I, KRAS WT, RIT1 WT

WAC_T457, RTN4_S107, CDK11B_S713, CTNND1_S4, NCOR1_S2212, KIAA1671_S1441, SUGP2_S291, CSNK1E_S408, USO1_S48, EIF3G_S264, MISP_T160, ATP2B1_S1127, PDE8A_S359, MYO9B_T1353, LRRC1_S456, AHNAK_S5293, DDX3X_S594, MGA_S969, BLM_T766, PRCC_S157, EXOSC7_S177, BEND3_T123, MCM2_S40, ZDHHC5_S409, PLEKHG3_S433, ERC1_T38, NFU1_S33, SLC9A1_S796, SAFB2_S207, AHNAK_S539, EPB41L5_S436, DSP_S165_S176_S178, HNRNPDL_S8, SLC4A7_T442, MACF1_S7455, GNG12_S41, LUC7L3_S449, AFF4_S836, ENAH_S512, EGFR_S1026

Site LFC (-3, 0, 5)

e EGFR p-site LFC — KRAS G12V/Q61H, RIT1 M90I; T693, S991, S991_T993, S1026, S1039, T1041_S1045, S1042, S1070, T1078, T1085, S1166, Y1172

f LFC USO1 p-S48 — RIT1 WT, RIT1 Mut, KRAS WT, KRAS Mut

g LFC USO1 S48-p vs KRAS LFC — KRAS WT/mut, RIT1 WT/mut